J Therm Spray Tech (2017) 26:610–626
DOI 10.1007/s11666-016-0480-y

PEER REVIEWED

Process-Structure-Property Relationships for 316L Stainless Steel Fabricated by Additive Manufacturing and Its Implication for Component Engineering

Nancy Yang[1] · J. Yee[1] · B. Zheng[2] · K. Gaiser[1] · T. Reynolds[1] · L. Clemon[1] · W. Y. Lu[1] · J. M. Schoenung[2] · E. J. Lavernia[2]

Submitted: 1 May 2016 / in revised form: 15 August 2016 / Published online: 8 December 2016

Abstract We investigate the process-structure-property relationships for 316L stainless steel prototyping utilizing 3-D laser engineered net shaping (LENS), a commercial direct energy deposition additive manufacturing process. The study concluded that the resultant physical metallurgy of 3-D LENS 316L prototypes is dictated by the interactive metallurgical reactions, during instantaneous powder feeding/melting, molten metal flow and liquid metal solidification. The study also showed 3-D LENS manufacturing is capable of building high strength and ductile 316L prototypes due to its fine cellular spacing from fast solidification cooling, and the well-fused epitaxial interfaces at metal flow trails and interpass boundaries. However, without further LENS process control and optimization, the deposits are vulnerable to localized hardness variation attributed to heterogeneous microstructure, i.e., the interpass heat-affected zone (HAZ) from repetitive thermal heating during successive layer depositions. Most significantly, the current deposits exhibit anisotropic tensile behavior, i.e., lower strain and/or premature interpass delamination parallel to build direction (axial). This anisotropic behavior is attributed to the presence of interpass HAZ, which coexists with flying feedstock inclusions and porosity from incomplete molten metal fusion. The current observations and findings contribute to the scientific basis for future process control and optimization necessary for material property control and defect mitigation.

✉ J. M. Schoenung
julie.schoenung@uci.edu

[1] Sandia National Laboratories, Livermore, CA 94551, USA

[2] University of California, Irvine, Irvine, CA 92697, USA

Keywords additive manufacturing · dendritic · LENS® · porosity · stainless steel

Introduction

Emerging additive manufacturing (AM) technologies, such as 3-D laser engineered net shaping (LENS), a commercial direct energy deposition (DED) (Ref 1), is capable of building complex engineering components to its final shape, dimension and surface finishing (Ref 2). 3-D LENS deposition involves instantaneous metal melting, molten metal flow, and solidification; in many aspects, the LENS deposition is similar to well-understood processes including metal casting, welding, and thermal spray. However, the manufacturing algorithm for building complex net-shaped engineering components (through multi-pass deposition of molten metal) is unique, and the resultant bulk material properties of the finished component are not yet fully understood (Ref 3, 4). For instance, the metallurgical reaction induced by the systematic interpass re-melting during the successive layer deposition is yet to be determined. In addition, for a component with a complex geometry, a scientific understanding is yet to be gained on how deposition dimensions, and/or hatch pattern motion can alter local thermal transport and heat distribution, and therefore the local physical metallurgy. In order to achieve the ultimate assurance in material properties and manufacturing consistency, process-structure-property relationships for 3-D LENS process must be established. In this study, we interrogate the physical metallurgy (mainly solidification microstructure, tensile properties, and Vickers microhardness) and discuss their correlation.

Experimental Materials and Methods

Materials—Starting Feedstock Powders

For the present study, 316L stainless steel powders processed by Carpenter Powder Products using gas atomization were used. The powder particles exhibited spherical morphology with a size range between 44 and 149 μm (Fig. 1). The nominal chemical composition, as supplied by the vendor, is listed in Table 1. XRD analysis (not shown here) showed that the feedstock powders are of the γ- austenitic phase.

3D LENS Deposition Process

The 3-D LENS depositions were performed with a 750 LENS® system (Optomec, Inc. Albuquerque, NM, USA) which consists of a continuous wave (CW) mode Nd:YAG laser operating up to 650 W at 1064 nm, a four-nozzle coaxial powder feed system, a controlled environment glove box, a motion control system, and real-time molten pool sensor (MPS) and Z-height control (ZHC) subsystem. Successive layers were deposited in the following order: first, a contour line that outlines the component is deposited; and second, the space within the contour outline is filled in with successive passes that are patterned in a hatched configuration. From layer to layer, the angle between each hatch pattern is 90°. A schematic of the building scheme is shown in Fig. 2. The layer thickness, hatch spacing, and work distance (from end of nozzle to the deposited surface) were set at 0.25, 0.39, and 9.5 mm, respectively. The main processing parameters used for the present study, including laser output power, traverse speed, and powder feed rate, are summarized in Table 2. The entire process was carried out in Ar environment to avoid oxidation during deposition. The oxygen level in the glove box was maintained about 15 ppm during depositions. The physical dimension and shape for the three prototypes are 24.5 mm × 12.3 mm cylinder, 12.3 mm × 4 mm thin disk and 50 mm × 50 mm 3-tier hexagon with 56 mm × 40 mm × 54 mm steps (shown in Figs. 2 and 3).

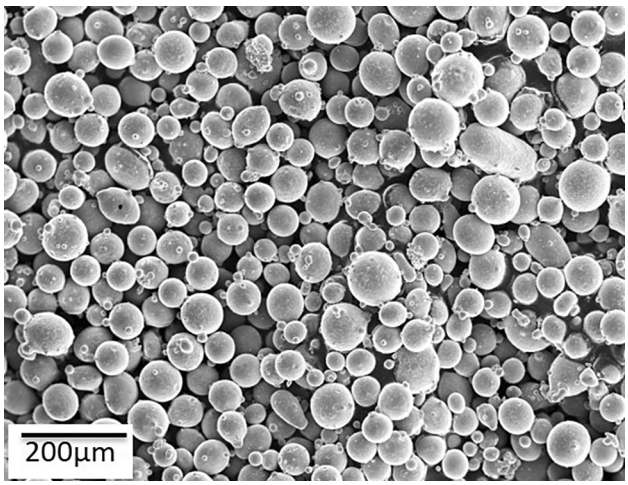

Fig. 1 SEM/SEI micrograph reveals the morphology for the 316L powder feedstock

Metallographic Sample Preparation

The 3-D prototype samples cross section were polished starting from 600 grit SiC paper down to the final finish using 0.05 μm colloidal silica. For microstructural characterization purposes (specifically to reveal the solidification microstructure), the final polished cross sections were also electrochemically etched using aqueous 60% nitric acid at 0.8 V.

Material Characterization Techniques

1. *Surface topography*

Surface contour and roughness were examined using scanning electron microscopes (SEM) with secondary electron imaging (SEI) or backscattered electron imaging (SEM/BEI), operated at 15 kV, and profilometry.

2. *Microstructure and crystal orientation*

Complementary optical microscope (OM) and scanning electron microscope SEM imaging were used to characterize the 3-D induced metallurgical features on the metallographically prepared cross sections. Solidification cell morphology and size were characterized using SEM with backscattered electron image (SEM/BEI) at 15 kV, and SEM with electron backscattered diffraction (EBSD) on the as-polished cross section.

3. *Vickers microhardness*

The measurement was conducted with a standard Vickers diamond indentation method using a 50-g load.

4. *Uniaxial tensile testing*

Round tension test specimens were machined from the multi-tier hexagon along the axial and transverse directions, as shown in Fig. 4. The length and diameter of the

Table 1 Nominal chemical composition for 316L stainless steel feedstock powder

Element	Fe	Ni	Cr	Mo	Mn	Si	C	P	S
wt.%	Balanced	10.3	16.3	2.09	1.31	0.49	0.026	0.026	0.006

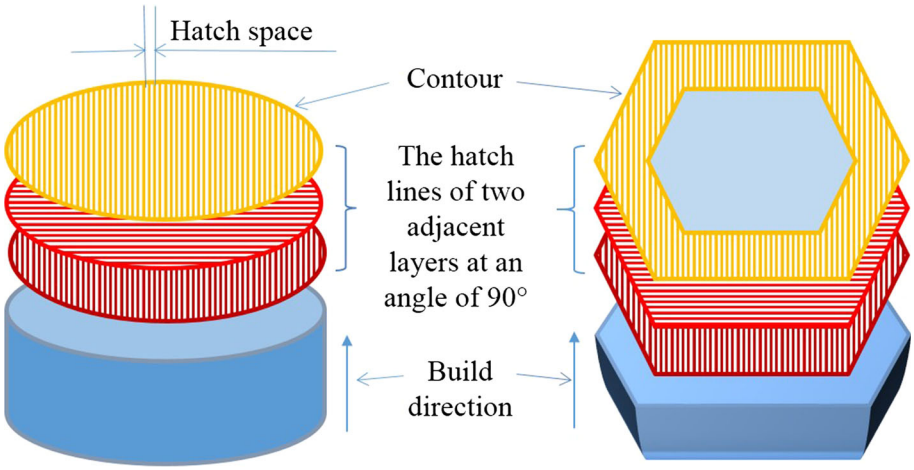

Fig. 2 Schematic of the deposition pattern for LENS deposited components

Table 2 Dimensions and processing parameters used of 3-D LENS prototypes

Part no.	Name	Dimensions (mm)	Laser power (W)	Current (A)	Speed (mm/s)	Feed rate (g/min)
1	Short cylinder	Ø24.5 × 12.3	360	38	16.3	10
2	Thin disk	Ø12.0 × 4.0				
3	Multi-tier hexagon	56 × 49 × 54				

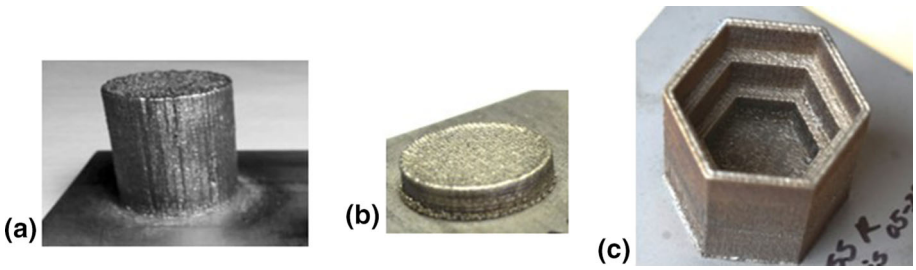

Fig. 3 Sample geometry of the 3-D LENS prototypes studied. (a) Part 1-1″ × 1″ cylinder; (b) Part 2-0.5″ × 0.16″ thin disk; (c) Part 3-2″ × 2″ 3-tier Hexagon

gage section were ~18 and ~2.5 mm, respectively. The test was quasi-static with a strain rate of 0.001 s^{-1}.

Experimental Results

Surface Topography

Surface contours and morphology among all the current 3-D LENS 316L stainless steel deposits are consistent, regardless of prototype geometry and dimensions. Complementary SEI/BEI images show that the deposit surfaces contain alternating layered ridges, originating from the multi-pass deposition (Fig. 4). Within each ridge, there are curved molten metal trails (Fig. 4—lower right arrows) perpendicular to the interpass boundaries, similar to the morphology seen in the metal welds. In addition, the surface also contains un-melted or partially melted particles, which are fused to the deposit surface and tend to gather along the molten metal flow trails and/or interpass boundaries. In many cases, several particles were fused together without direct contact with the surface. The size and shape of these fused-on particles are comparable to that of the 316L feedstock powders used for the current 3-D LENS deposition (Fig. 5-upper left insert). The profilometry map (Fig. 6-upper map) shows a relatively rough surface, average ~300 μm deep from peak to valley. This depth was verified quantitatively by profilometry profile (Fig. 6-upper profile). This process induced rough surface (≥300 μm) is about 2-3 times higher than those measured from those parts finished by a conventional mechanical machining (Fig. 6—lower profile). The rough surface features created by 3-D LENS may act as stress concentrators and serve as origin point for potential failure in AM engineering components. This effect would be particularly amplified in thin members, where the effective surface layer is a larger proportion of the entire volume of the component. In conventional engineering components, these

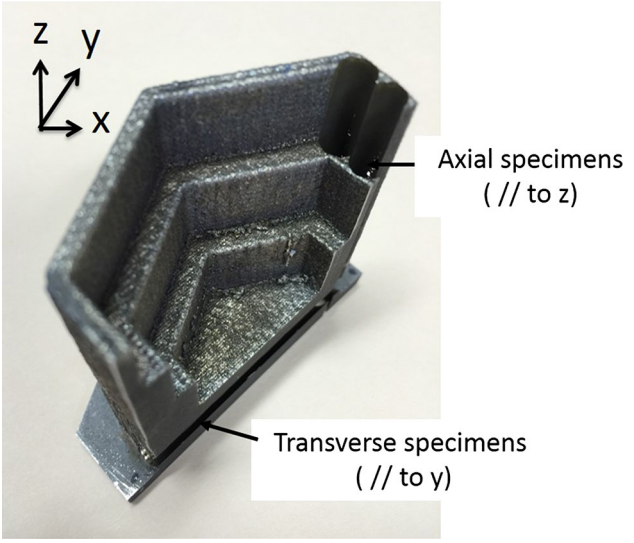

Fig. 4 Tensile specimen orientation and designation for samples machined from 3-D LENS hexagon

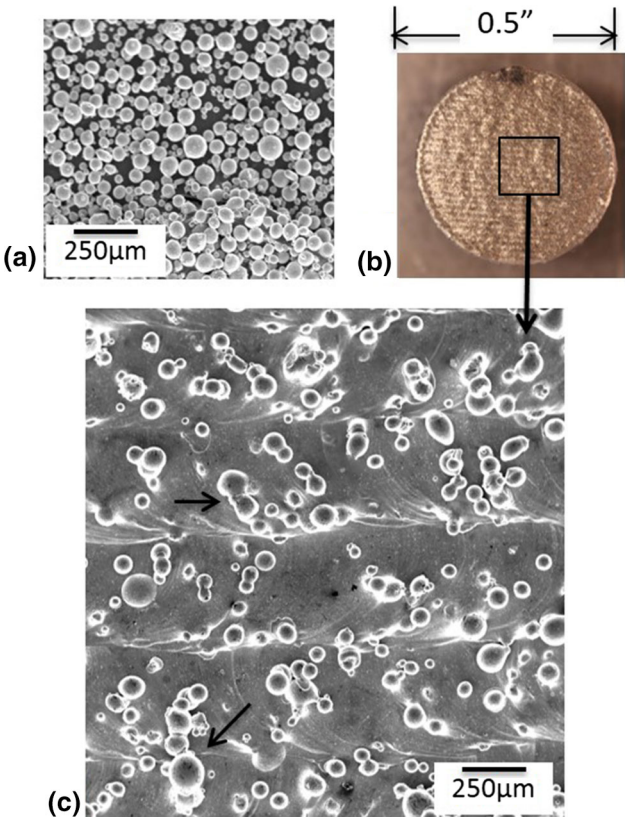

Fig. 5 SEM/SEI micrographs compare the morphology between the 316 L feedstock powders and un-melted powders fused on the 3-D LENS deposit. (a) Feedstock powders; (b) modulated surface on 3-D LENS Part 1; (c) un-melted powders on 3-D LENS deposit

features are often mitigated through fine surface finishing; however, this may not be afforded to all engineering AM components that are deployed.

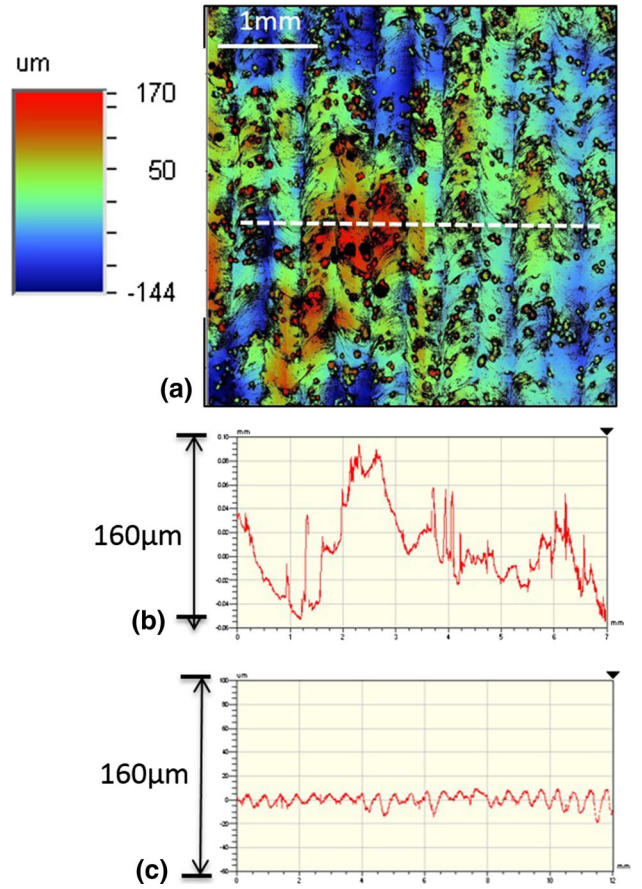

Fig. 6 Surface contour and topography quantified using profilometer. (a) Contour map; (b) surface profile for the 3-D LENS thin disk (Part 2), along the dot line drawn in 4a above; (c) surface profile for the mechanically finished surface

Microstructural Characteristics

1. Part 1—Short cylinder

The optical micrographs show minimal gross structural defects, i.e., porosity in particular, in the bulk as-polished or chemically etched cross section (Fig. 7—upper right box). The etched cross section shows a mesh-like morphology, which contains light contrasted horizontal and vertical curved thin interfaces (Fig. 7-lower). This mesh-like morphology is consistent throughout the entire deposit. However, the dark field optical micrograph shows gross structural defects within 3-4 mm from the substrate interface and ~1-2 mm from the free sidewall surface (Fig. 7—upper right arrows).

At the middle of the cylinder, the enlarged optical micrographs show that the light contrasted vertical and horizontal interfaces that correspond to the molten metal flow trails and interpass boundaries respectively (Fig. 8—area 1 and 2). The morphology of both types of interfaces often is erratic or irregular, especially at the triple junctions

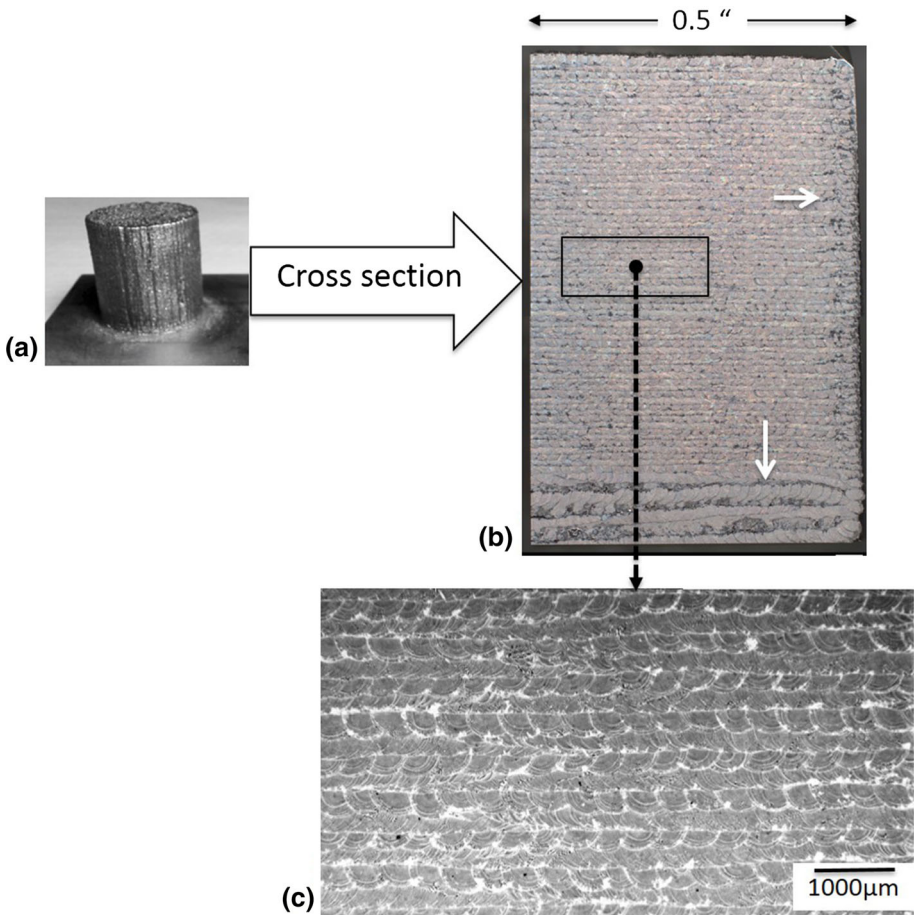

Fig. 7 Optical micrographs for 3-D LENS Part 1. (a) 3-D as-deposited; (b) etched cross section by dark field (DF); (c) etched cross section by bright field (BF)

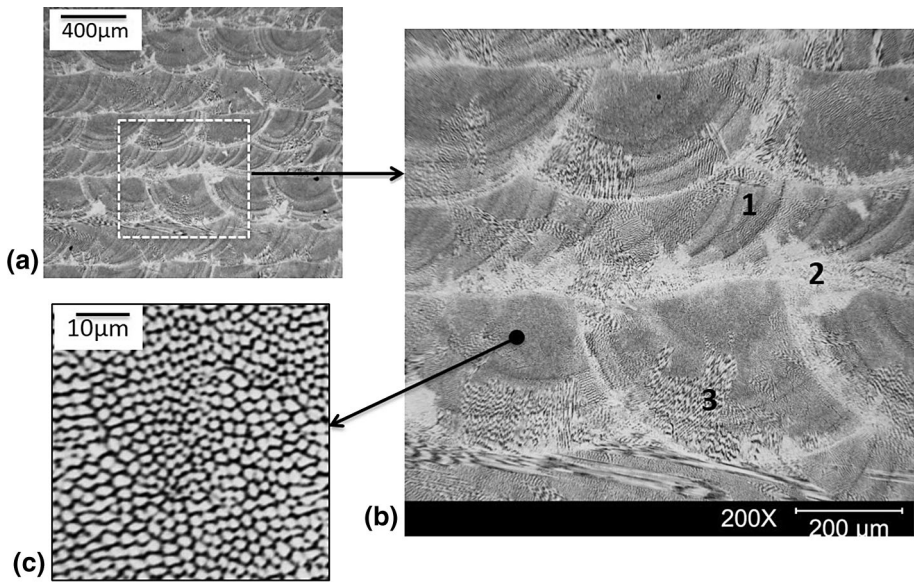

Fig. 8 OM/BF micrographs of the chemically etched cross section. (a) Area of interest; (b) the three distinct microstructural features: 1, 2 and 3; (c) the fine detail microstructure inside the solidification cell

between the interpass boundaries and metal flow trails, where the light contrasted features are much more revealing or massive (Fig. 8-area 2). Randomly oriented solidification cells between the interpass boundaries contain finely spaced secondary dendritic arms, less than 5 μm (Fig. 8—area 3 and lower left inset). The optical micrograph (Fig. 9) shows the light contrasted triple junctions that represent localized HAZs, which consist of less

defined re-solidified fine dendritic cells (Fig. 9—lower right). Sub-micrometer speckles were also observed at the secondary dendrite arm boundaries. Phase identification of these speckles has yet to be determined; this could possibly be a residual ferritic phase, oxides, and/ or gas bubbles (Fig. 9). We also noticed that solidification cells, in many cases, are interwoven with the molten metal flow trails, but the solidification cell growth usually is limited to the interpass boundaries (Fig. 9-lower left). Most importantly, the metal flow trails and interpass boundaries appear to be well fused and often connected with epitaxial interfaces. In addition to the fine speckles observed in the localized HAZ, we also detected sub-micrometer features, presumably gas bubbles or oxides, dispersed throughout the deposit (Fig. 10). The chemical composition or phase identification of the fine dispersions is to be determined.

At the top surface of the etched cross section, there are fused-on particles, either un-melted (Fig. 10-right) or partially melted (Fig. 10-left), which are the cross section of those surface powders seen in Fig. 3. The fused-on particles mostly reside on the deposit surface either above or nearby the molten metal flow trail (Fig. 10-circles). Underneath the fused-on powders, there are light contrasted localized heat-affected zones (HAZ), similar to those seen in the bulk, described in Fig. 10. The HAZ also contains poorly defined re-solidified dendritic structure mixed in with some recrystallized coarse grains as well as fine speckles (Fig. 11- lower insert).

2. Part 2—Thin disk

We also observed the modulated features and un-melted particles deposited on the surface (Fig. 12-left) and a mesh-like morphology on the etched cross section, which were outlined by the light contrasted HAZ as described earlier in Fig. 7 for the bulk cylinder (Fig. 11-right). The morphology, size, and distribution for the solidification cells were examined using complementary OM/BEI/EBSP images (Fig. 13). The OM/BEI/EBSP images show the solidification cells possess high aspect ratios (20-30 μm wide × 100-200 μm long) and are curved and stacked up horizontally between interpass boundaries (Fig. 13). SEI/BEI and EBSP images (Fig. 13) show solidification cell size (length in particular) and are confined within the

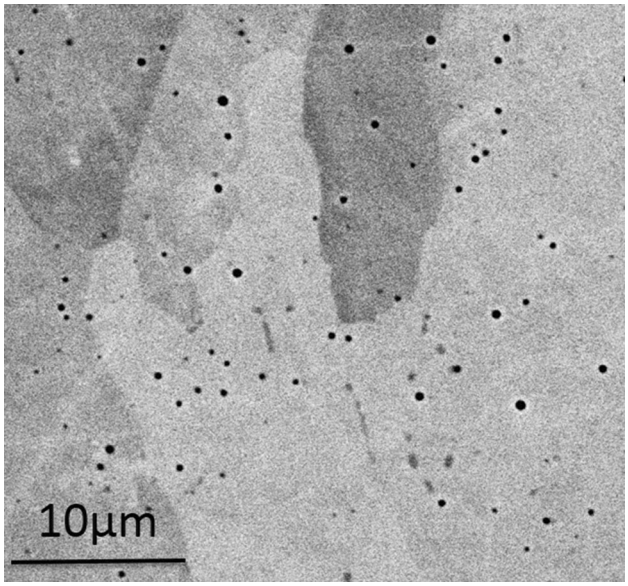

Fig. 10 SEM/BEI micrograph of fine dispersions

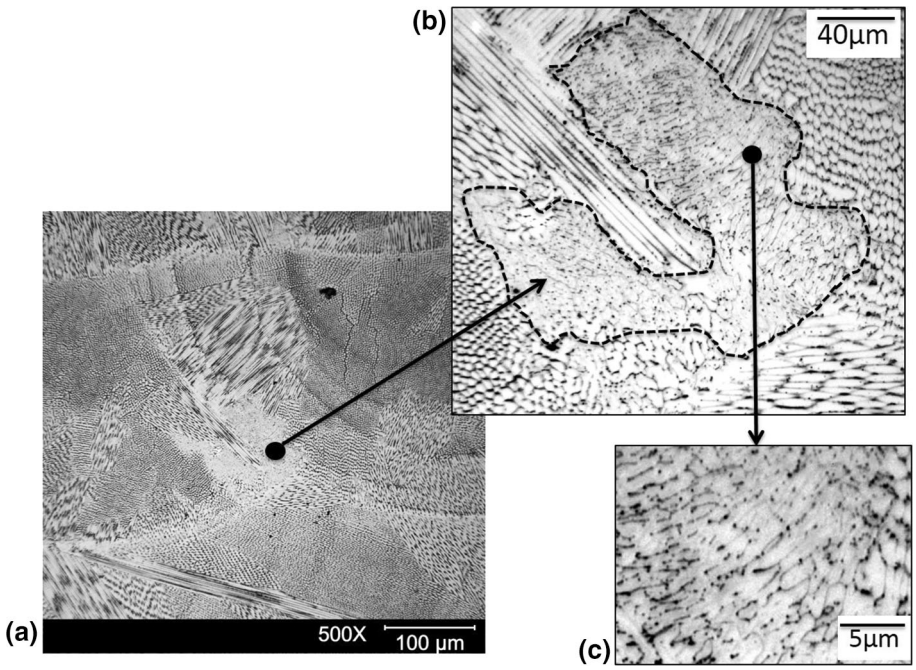

Fig. 9 OM/BF micrographs: (a) interpass HAZ; (b) enlarged micrograph of HAZ; (c) detail microstructure inside the HAZ

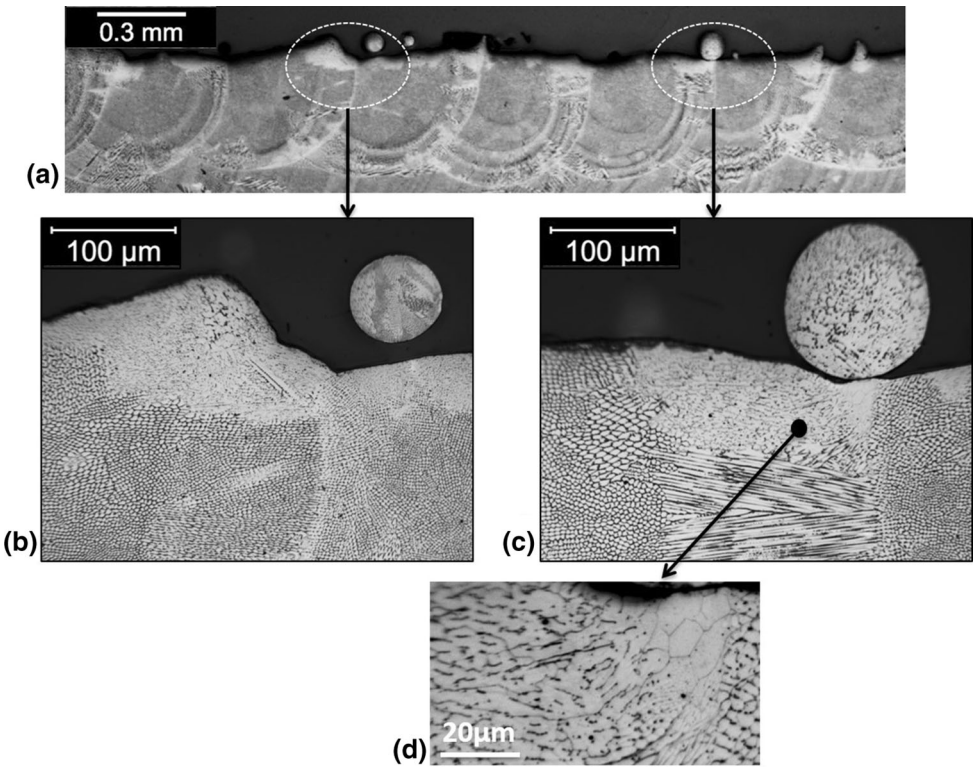

Fig. 11 OM/BF micrographs for the etched Part 1. (a) Area of interest (circles); (b) HAZ under the partially melted powder; (c) HAZ under the un-melted powder; (d) enlarged micrograph reveals the fine detail inside the HAZ

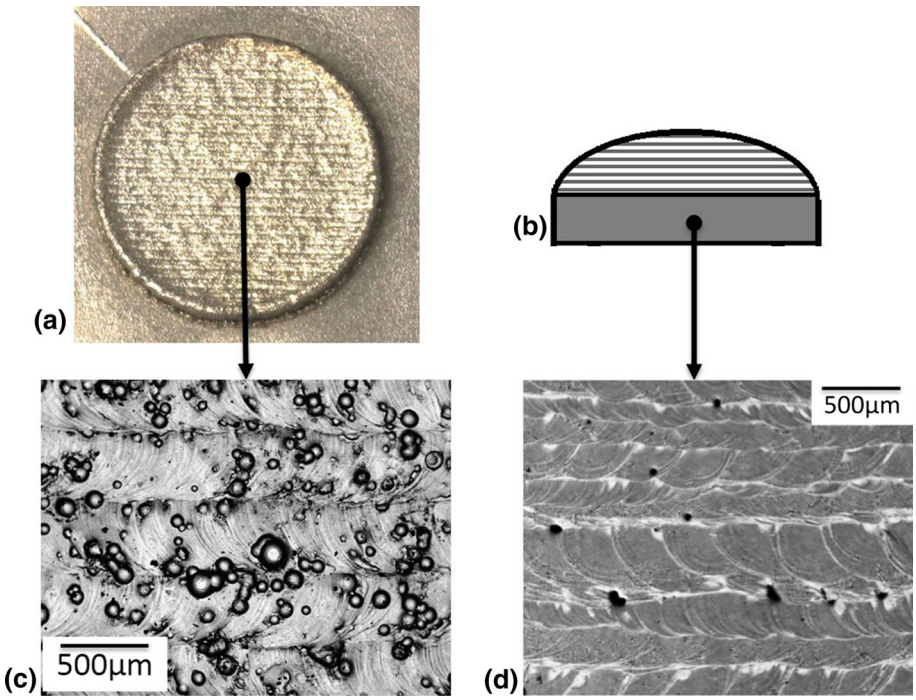

Fig. 12 (a) Digital photo of the modulated deposit surface; (b) Schematic of the thin disk cross section; (c) SEM/BEI micrograph of the un-melted powders on 4-mm thin disk (Part 2); (d) OM/BF micrograph of the cross section with mesh-like morphology

thickness of each deposition layer. The interfaces were again well fused at interpass boundaries and metal flow trails, which were also interwoven with solidification cells (Fig. 14-arrows).

It should be noted that the current 4-mm thin deposit contains unusually high interpass porosity and partially melted particle inclusions. The size and shape of the inclusion resemble those 316L feedstock powders shown in Fig. 5. In most cases, the interpass pores appear to coexist with the un-melted or partially melted 316L particle inclusions (Fig. 15). In addition, the deposit contains coarse crystalized grains at the interpass boundaries and/or

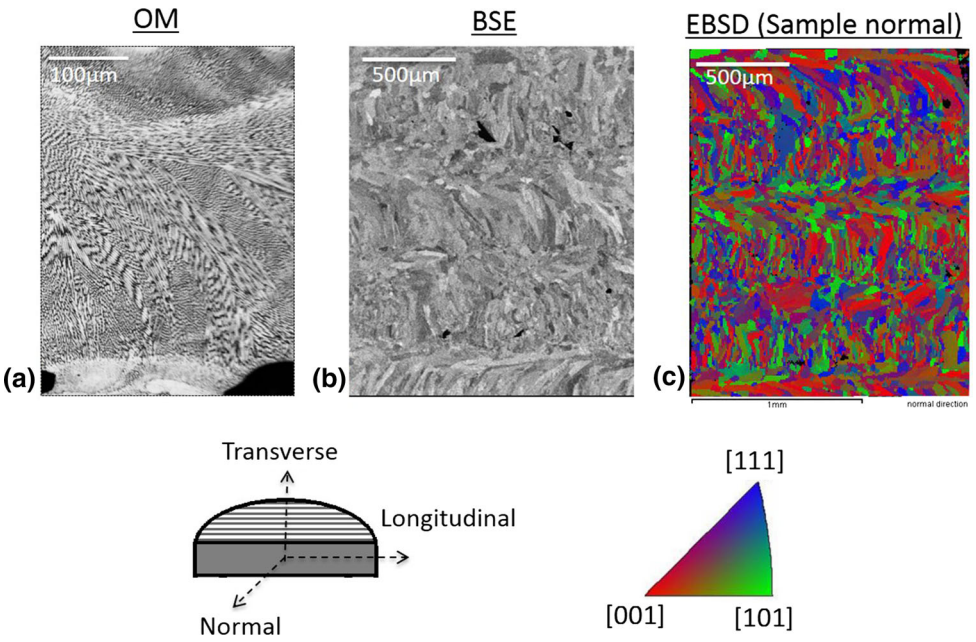

Fig. 13 Morphology, size and crystal orientation for the solidification cells. (a) OM/BF micrograph; (b) SEM/BEI micrograph; (c) EBSP orientation map. The lower figures are the definition for deposit orientation (left) and color code for crystal orientation (right)

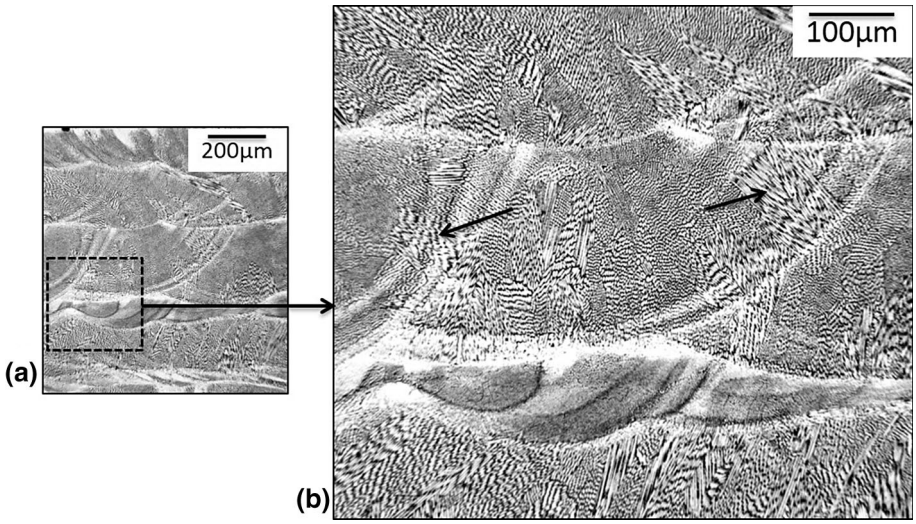

Fig. 14 OM/BF micrographs reveal the typical solidification microstructure for Part 2. (a) The area of interest; (b) interface fusion and solidification cell/molten metal flow interaction (arrows)

surrounding the partially melted interpass inclusions (Fig. 15 and 16). These interpass defects seem to be consistent with our observations of the bulk cylinder, which contained a high concentration of the same defects within the first 4-5 layers of the deposition. The formation of these defects could be a result of large thermal gradients between the molten metal being deposited and the cold substrate, where many un-melted inclusions become the origin of the gross interpass porosity. Additionally, it is noted that the nanoscale dispersions also found throughout this thin deposit are similar to those seen in Fig. 10.

3. Part 3—Multi-tier hexagon

The cross-sectional view and the dimension of the multi-tier hexagon are shown by the following schematic (Fig. 16). Again, the mesh-like morphology also seen in all tiers with exception of the thin Tier 1 where the interpass boundaries are not well defined (Fig. 17-upper left). In addition, the narrow Tier 1 deposit contains centerline porosity. It should be noted that centerline porosity appeared to extend continuous down to the base, $\sim$1 mm from the free sidewall surface (Fig. 17-upper left). For the other tiers and the base, the microstructural characteristics are generally consistent with the mesh-like morphology described earlier for the inch-size bulk or 4 mm thin deposit in Fig. 8 and 12. However, this hexagon contains moderate amounts of gross interpass pores and partially melted 316L inclusions, as indicated in the light contrasted interpass boundaries, especially within 4-5 mm from the substrate interface (Fig. 18). The high-magnification

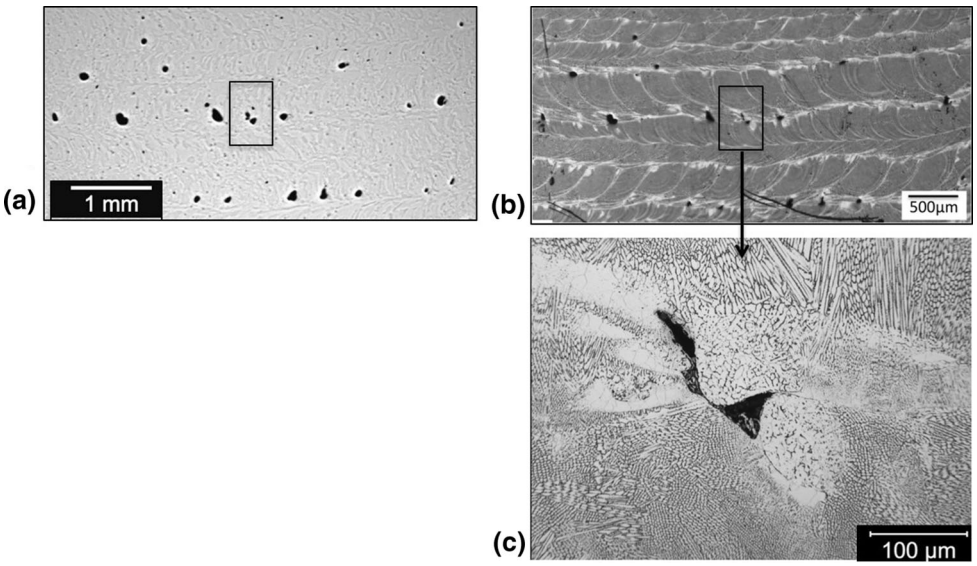

Fig. 15 OM/BF micrographs of the gross interpass defects. (a, b) Area of interest revealed before and after chemical etching; (c) un-melted powder-pore interaction

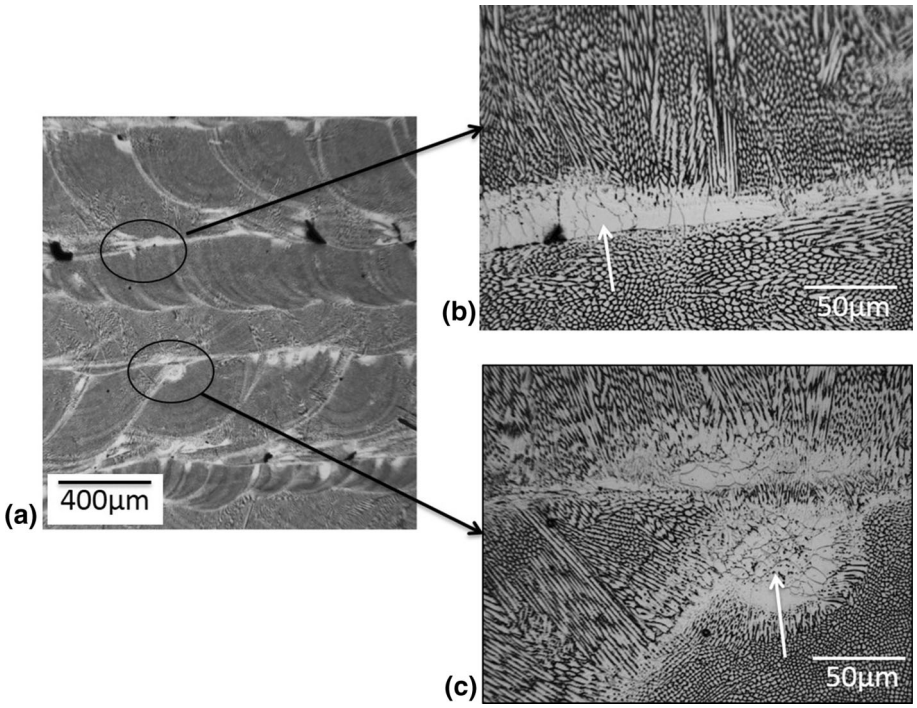

Fig. 16 OM/BF micrographs: (a) area of interest; (b) interpass boundary with coarse recrystallized grains (light arrow); (c) interpass with an un-melted powder inclusion (light arrow)

optical micrographs also revealed the presence of interpass recrystallization and grain growth, either surrounding the partially melted inclusions and/or along the interpass boundaries, similar to those found earlier in Fig. 17 (Fig. 19). We also note that the delta ferrite content in the current prototypes (including the short cylinder, thin disk, and 3-tier hexagon) ranges between 0.2-0.5% as measured by eddy current measurements, which is much less than the wrought substrate material (1-3% ferrite) (Fig. 20).

Another important finding is that the solidification cell structure appears to increase with the size with increasing distance from the substrate interface from the base to Tier 1, with descending deposit width (Fig. 21). As with the other wide 3-D LENS deposits, the solidification cell growth is constrained at the interpass boundaries.

Mechanical Properties

1. *Vickers microhardness*

200 Vickers microhardness measurements (Fig. 22-left) show large variations among the different locations (Fig. 22-right). The average Vickers microhardness was 260 HV, which is 15-20% harder than the listed nominal

Vickers microhardness [(222 HV) for wrought 316L stainless steel] (Ref 5). The calculated standard deviation is ±14 HV, compared to ±9 HV measured in the wrought 316L substrate. In addition, the average Vickers microhardness from the 5-point measurements for all tiers shows the hardness decreases with increasing distance from the substrate interface, from the base to narrow Tier 1 (Fig. 23).

2. *Tensile properties*

Tensile testing was performed for the four specimens, two for axial and two for transverse direction, taken from the 3-D LENS hexagon (Fig. 4). The stress-strain curves (Fig. 24) show yield strength for the two axial specimens is 448 and 455 MPa, which is 15-20% lower than those measured for two transverse specimens, which is

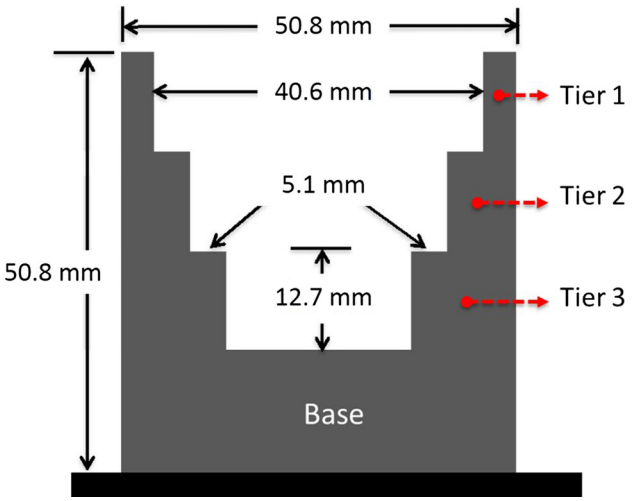

Fig. 17 Schematic and nominal dimensions of the 3-D LENS hexagon cross section

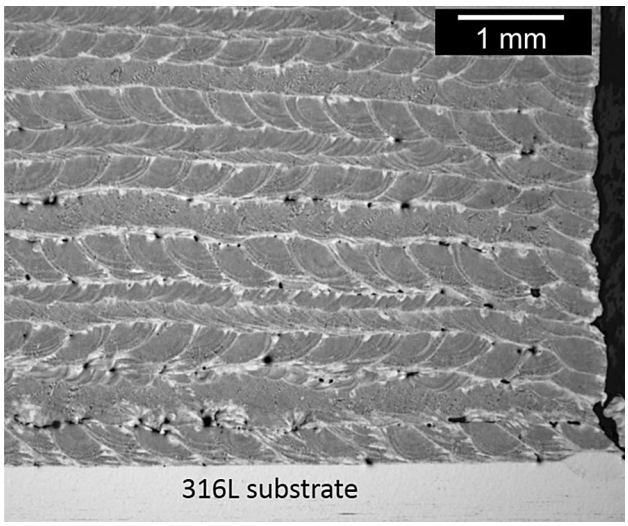

Fig. 19 OM/BF micrograph reveals gross interpass defects within 3-4 mm from the substrate interface

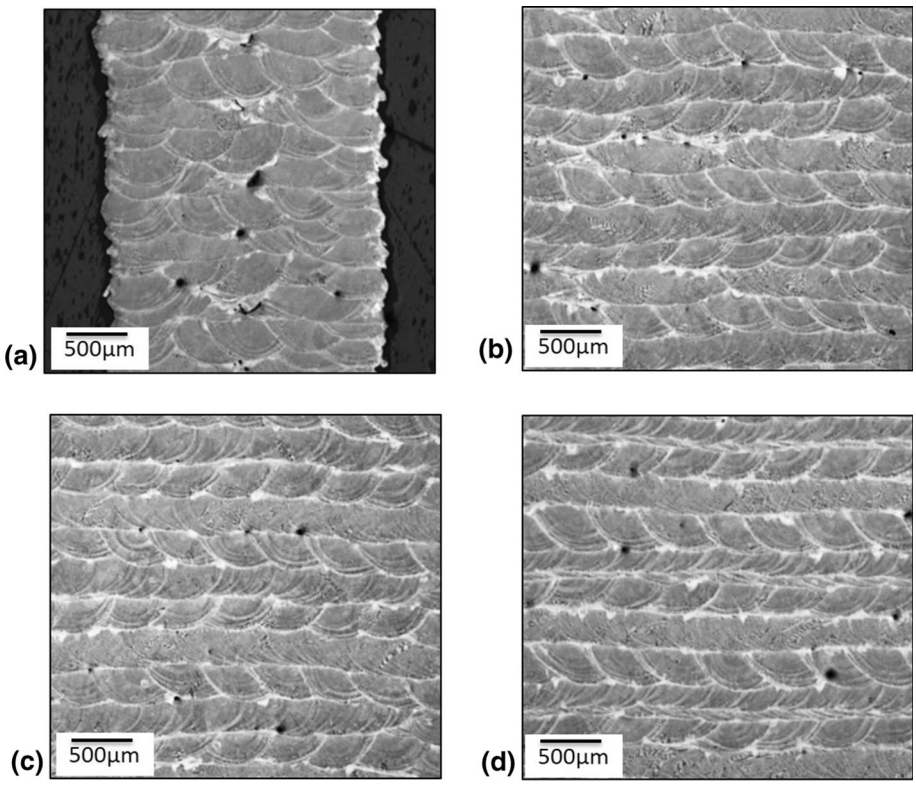

Fig. 18 Typical morphology on the chemically etched hexagon cross section. (a) Narrow Tier 1; (b) Tier 2; (c) Tier 3; (d) wide base

consistent, 538 and 552 MPa. The average ultimate yield strength (UTS) for the axial and transverse specimens is 586 and 690 MPa, respectively. Both the yield strength and the UTS for the 3-D LENS deposits are relatively higher than those listed nominal strength for the wrought 316L stainless steel (Ref 5). Most notably, the strain-to-failure measured among the four specimens varied greatly, ranging from 4 to 38%. The strain-to-failure was also found to be anisotropic, being lower for the two axial specimens. The overall tensile property measured for the four specimens are tabulated in Table 3. It should also be mentioned that the plastic regime of the stress-strain curves are relatively flat, indicating limited work hardening.

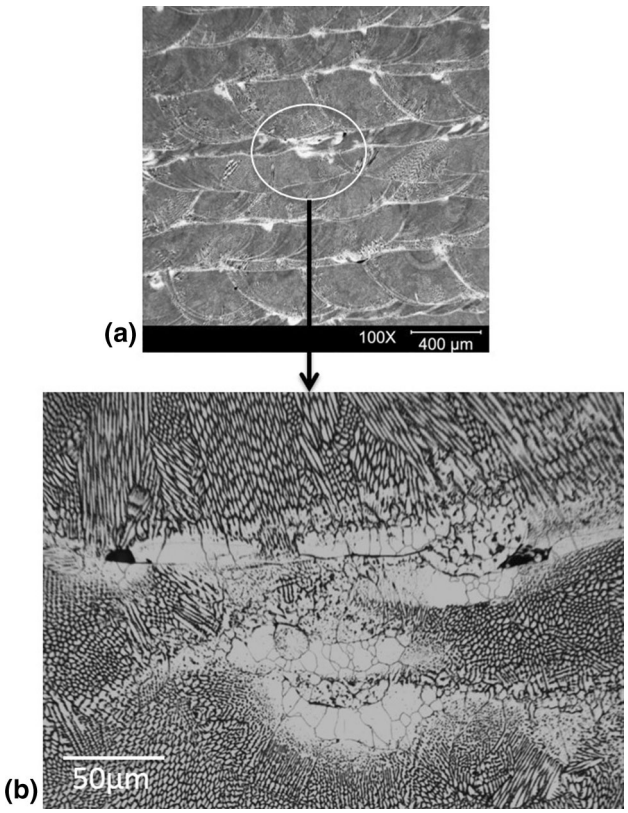

Fig. 20 OM/BF micrographs for the 3-D LENS hexagon. (a) The area of interest; (b) it reveals interpass defects with recrystallized coarse grains and pores

3. *Fractography*

Tensile fracture surfaces were examined using SEM/SEI imaging. All four specimens failed near mid-length of the gauge section, which corresponds to ~13 mm between the Tier 2 and Tier 3 of the hexagon. The fracture behavior between the two specimens for each direction in general is consistent with each other. However, specimens from the axial and transverse directions exhibit very different tensile deformation characteristics. The axial specimens displayed little tensile elongation or necking, while the transverse specimens displayed ductile elongation or necking (Fig. 25-upper). In addition, the fracture surface of the sample taken from the axial orientation exhibited interfacial delamination at the interpass boundaries that contains HAZ and gross defects with un-melted particle inclusions and featured a smooth unfused surface (Fig. 25-lower). On the other hand, the two specimens that were taken from the transverse orientation exhibited typical ductile failure, featuring a dimpled fracture surface. The dimple cell size observed on the fracture surface(s) of these samples was extremely small, smaller than 5 μm; these are comparable to the fine cellular arm spacing (CAS) shown in Fig. 7. It is also worth mentioning that the SEM/SEI micrograph of the side of the transverse specimens shows signs of thin secondary ductile tearing, perpendicular to the tensile loading direction (Fig. 26).

Discussion

The physical metallurgy observed in the present investigation is derived from systematic metallurgical reactions from multiple passes of coaxial powder feeding and molten metal deposition. The following discussion contains some of the scientific rationale behind the correlation between the 3-D LENS process, microstructural features, and engineering properties.

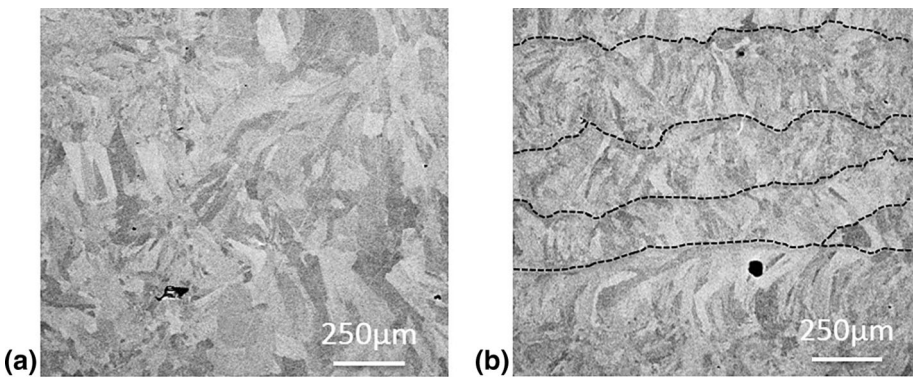

Fig. 21 SEM/BEI micrographs reveal the solidification cells. (a) The narrow Tier 1; (b) the wide base with interpass boundaries

3-D LENS Induced Solidification Microstructure and its Impact on the Tensile strength

It is well established that solidification microstructure is closely related to the cooling rate. It is also suggested that at a given bulk alloy composition, the solidification microstructure can evolve from planar to cellular to dendritic with faster cooling rates (Ref 6-9). We expect that rapid cooling during the 3-D LENS process is analogous to that of welding, which seems to be consistent with our observations in the present investigation on the metallurgical evolution and resultant microstructure, i.e., cellular morphology with a fine cellular arm spacing (CAS) (Ref 7).

It is also found that for a bulk deposit (greater than 2 mm wide), the primary solidification cell growth is influenced by the presence of interpass boundaries. The size of high aspect ratio solidification cell appears terminated at the interpass boundaries. Additionally, the material is susceptible to a systematic interpass HAZ, which in most cases contains a mixture of recrystallized coarse grains and/or poorly defined mushy zone due to a reheating and re-melting from the successive layer deposition. In general, we observed the presence of these interpass HAZ-type defects in all of the bulk (e.g., thick) 3-D LENS deposits, particularly in the areas surrounding un-melted/partially melted particles. On the other hand, the narrow deposit (less than 2 mm wide) exhibits much coarser primary solidification cells, both in width and length, due to the absence of interpass boundaries as shown in Fig. 17.

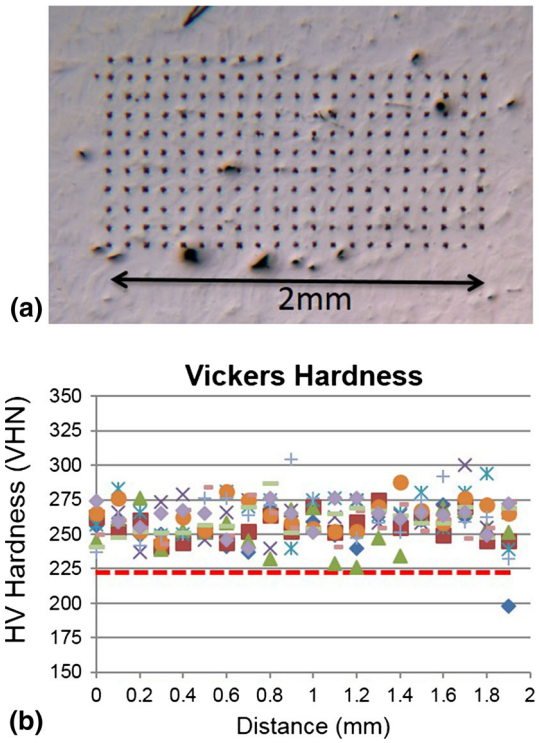

Fig. 22 (a) OM/BF micrograph superimposed with Vickers diamond indents; (b) Vickers hardness plot from the location shown in Fig. 21(a)

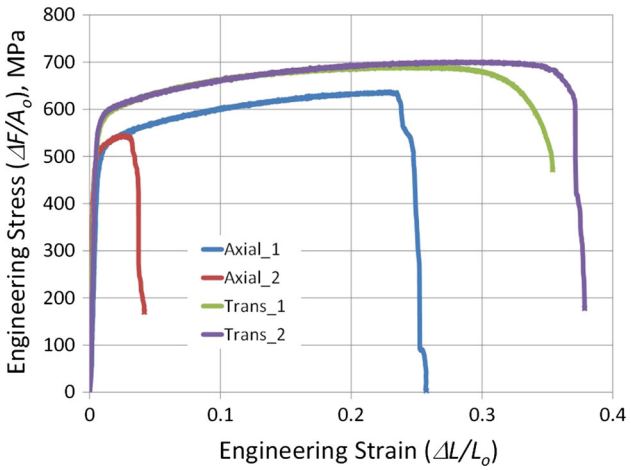

Fig. 24 Stress-strain curve for the four tensile specimens taken from the 3-D hexagon

Fig. 23 Vickers hardness measurements. (a) 15-point of each tier at an equal distance, bottom to top; (b) Vickers hardness change with Tier number based on the 15-point average from those measurements shown in Fig. 23(a)

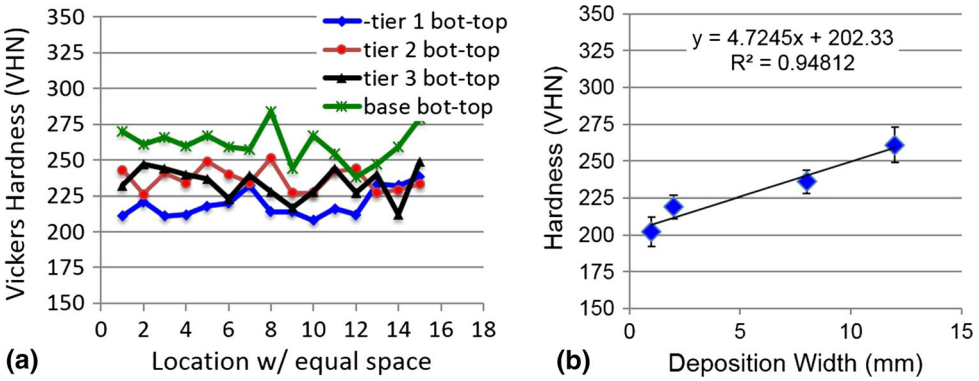

Table 3 Summary of mechanical properties of 3-D LENS multi-tier hexagon

	Yield strength (MPa)	UTS (MPa)	Strain-to-failure (%)	Vickers microhardness (HVN)
Wrought 316L (Ref 5)	170	450	40	222
316L hexagon axial 1	455	634	25	Base: 260
316L hexagon axial 2	448	545	4	Tier 1: 220
316L hexagon trans 1	538	690	35	
316L hexagon trans 2	552	703	38	

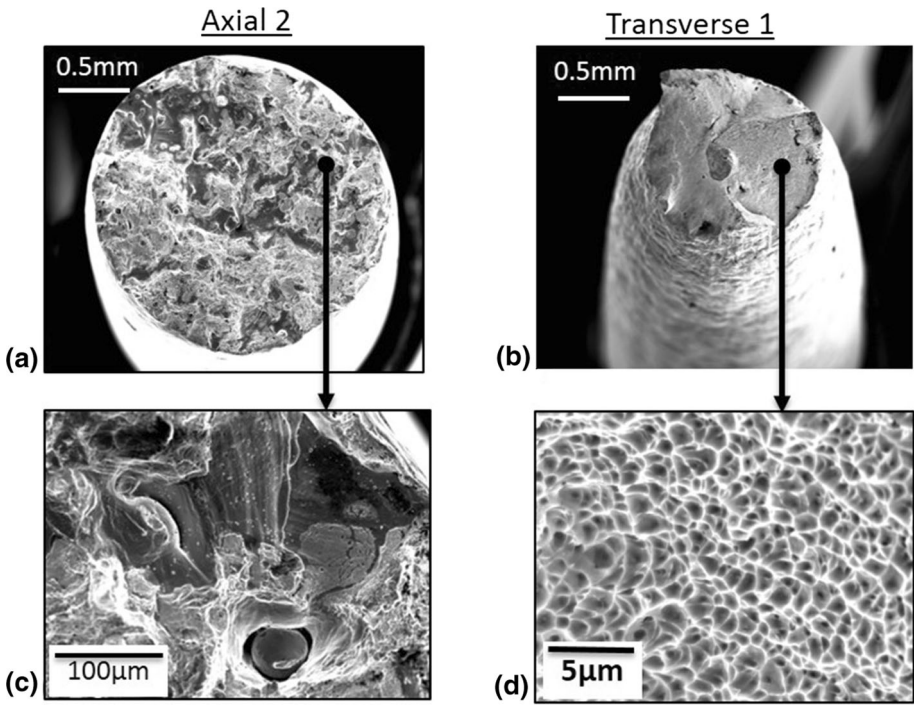

Fig. 25 SEM/SEI micrographs of the tensile fractured faces. (a) Axial 2 at low magnification; (b) Transverse 1 at low magnification; (c) Axial 2 at high magnification; (d) Transverse 1 at high magnification

We believe that the fine CAS by fast cooling is responsible for the high yield strength, UTS and Vickers hardness measured for the current 3-D LENS prototypes compared to wrought material (Ref 5); these trends are consistent with a Hall-Petch type relationship with mechanical properties and solidification cell size (Ref 10, 11). The similar argument could be made to explain the low Vickers hardness of narrow deposit at Tier 1, without interpass boundary, where the primary solidification cells are much coarser.

Surface Morphology and Its Implication to Structural Integrity

The surface of a component produced by 3-D LENS is susceptible to un-melted feedstock powder deposition during the powder feeding/molten metal deposition and solidification process (Fig. 27). Majority of the un-melted powders were fused tightly onto the deposit surface; in many cases, multiple particles fused with each other beyond the deposition surface (Fig. 27—upper right). These fused-on un-melted powder particles not only modify the ultimate surface roughness, but also become a source of interpass inclusions if they remain un-melted, and ultimately the root cause of adverse interpass porosity (Fig. 27). The likely mechanism for interpass pore formation is illustrated by the schematic in Fig. 28, which suggests that the pore originates from incomplete metal fusion. Here, the metal flow is interrupted by the presence of an un-melted solid inclusion. Furthermore, the interrupted metal flow appears to change the heat transfer and flow dynamics of the process, resulting in the formation of

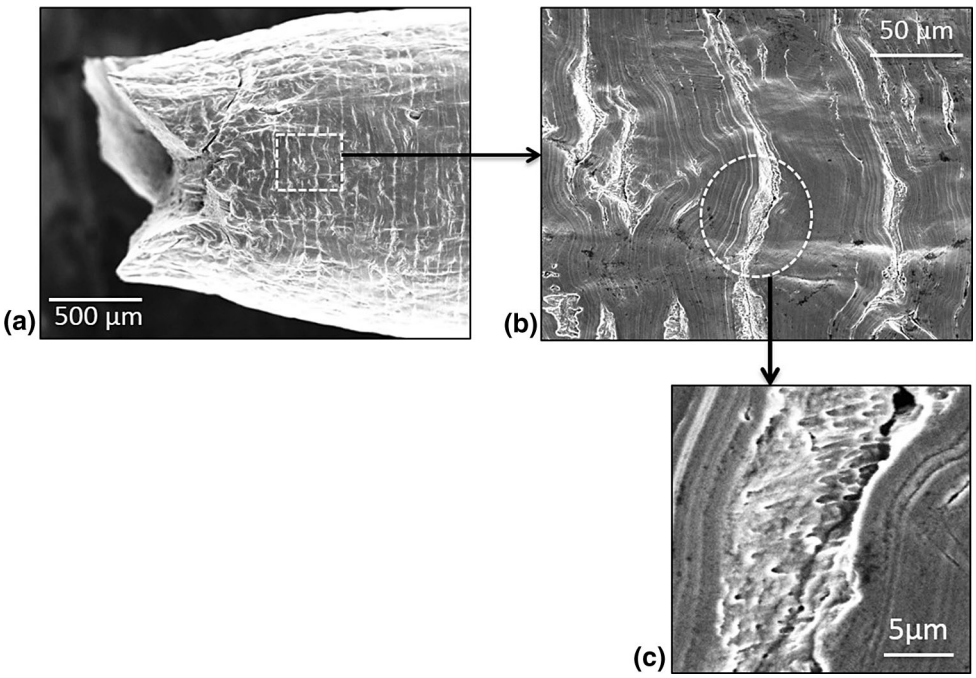

Fig. 26 SEM/SEI micrographs of reveal the systematic secondary tensile cracks on the side view. (a) Area of interest; (b-c) progressive enlarged micrographs show ductile tearing at the secondary tensile cracks

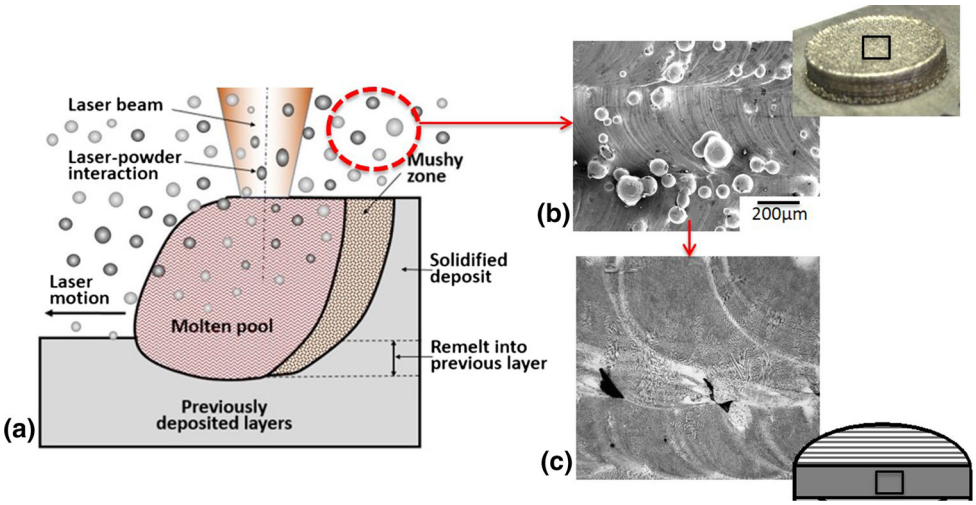

Fig. 27 Correlation among powder feeding, surface topography and structure integrity for 3-D LENS deposition. (a) Schematic of 3-D LENS deposition algorithm; (b) SEM/SEI micrograph of the fused-on un-melted feedstock powders; (c) OM/BF micrograph of the gross interpass un-melted powder inclusions and pores. Note: The right inserts are the area of interest on the surface and cross section

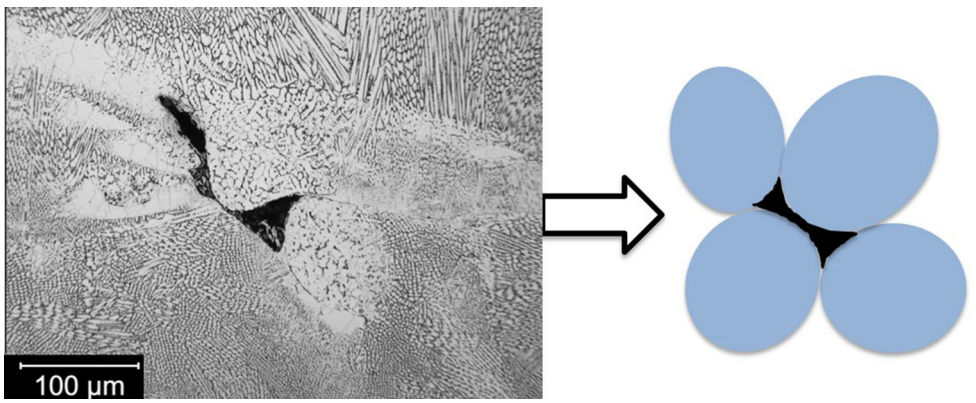

Fig. 28 Schematic illustrates the likely formation mechanism for the gross interpass defect observed

recrystallized grains within HAZs. We have observed in all of the prototypes produced by 3-D LENS that recrystallized grains within a HAZ seem to occur near porosity on the interpass boundaries. Additionally, the interpass porosity/gross interpass defects are usually more pronounced near substrate interfaces and/or free surfaces on the side of the deposition, possibly caused by large thermal gradients between the cold substrate, (or free surface on the side), and super-heated molten metal trace (Ref 12). It was also been suggested that the cause of the near sidewall porosity seen in Fig. 3 is related to the movement of the tooling, and spacing between the hatching/contour layers (Ref 13).

Effect of Microstructural Factors on Vickers Microhardness

In general, the Vickers microhardness of the 3-D LENS prototypes was higher than that of the equivalent wrought alloy. The increased hardness of the prototypes originates from the fine solidification cells, which has been reported for a variety of materials (Ref 7). Large variations of the Vickers microhardness were seen from the measurements taken at the hexagon base, as shown in Fig. 22. The standard deviation these hardness measurements is ±14 HV, which is ~35% larger than those measured from the 316L wrought substrate. The optical micrograph in Fig. 29, overlapped with the original 200 Vickers indentations, shows that the cause of the large hardness variation most likely is related to the heterogeneous microstructure, which contains the light contrasted interpass HAZ, interpass inclusions, large porosity, and recrystallized coarse grains (Ref 2, 14, 15). In general, Vickers microhardness measured in the interpass HAZ regions are softer and more variable due to the presence of porosity. In addition, residual stress development is an intrinsic outcome of successive deposition processes, such as 3-D LENS (Ref 2), which impact the properties of deposited materials (Ref 16, 17). The investigation of internal residual stress on mechanical behavior in the deposited structure is an ongoing effort by others. In addition, the experimental results show a possible correlation between the Vickers microhardness and deposition dimension, through the solidification cell size argument. The higher Vickers hardness measured in the narrow deposit in Tier 1 of hexagon is for its coarse solidification cell due to the absence of interpass boundaries as shown in Fig. 18, 19, and 21.

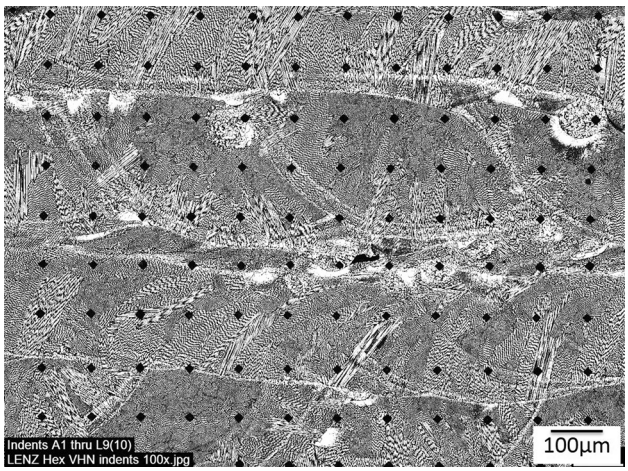

Fig. 29 OM/BF micrograph of the chemically etched cross section superimposed with 20 × 10 arrays of Vickers indents. Note the light contrast areas are HAZs and/or molten metal flow trails

Effect of Interpass Structure on Ductility and Tensile Failure

The stress-strain curve for the samples that originated from the multi-tier hexagon shows that the yield strengths and ultimate tensile strength (UTS) are relatively consistent between both the axially and transversely oriented samples. Most significantly, the stress-strain curve shows anisotropic tensile strain-to-failure between the axial and transverse loading direction. We also observed a large variation of the strain-to-failure between the two different axial specimens. The cause of the anisotropic tensile strain-to-failure and the large variation between the two axial specimens are rationalized by the following arguments related to interpass structure.

The interpass structure shown in Fig. 18, 19, 20, and 21 is commonly seen from the base to Tier 1 of the hexagon, i.e., the interpass HAZ with un-melted inclusions and pores were present randomly throughout the hexagon. For the transverse specimens, the interpass boundaries were subjected to shear stress. For the axial specimens, the tensile loading was parallel to the interpass boundaries, subject to normal tensile stress. The fractography shows the transverse specimens consistently failed by typical ductile failure with >40% strain-to-failure (Fig. 30—lower right), while the axial specimens failed by interpass delamination with <30% strain-to-failure (Fig. 30-lower left). This means that the tensile strength or ductility is much less sensitive to the presence of interpass HAZs with gross inclusions and large pores under tensile stress than to shear stress.

The large variation of the strain-to-failure observed between the two axial specimens is attributed to the non-uniform interpass microstructure throughout the hexagon (Fig. 31). The fracture surface of axial sample with higher strain-to-failure (~25%) approaches that of the Transverse sample #1 (~38%). This sample failed at the interpass boundaries (Fig. 31-lower), yet mostly by ductile tearing (as evidenced by the dimpling) with minimal interpass

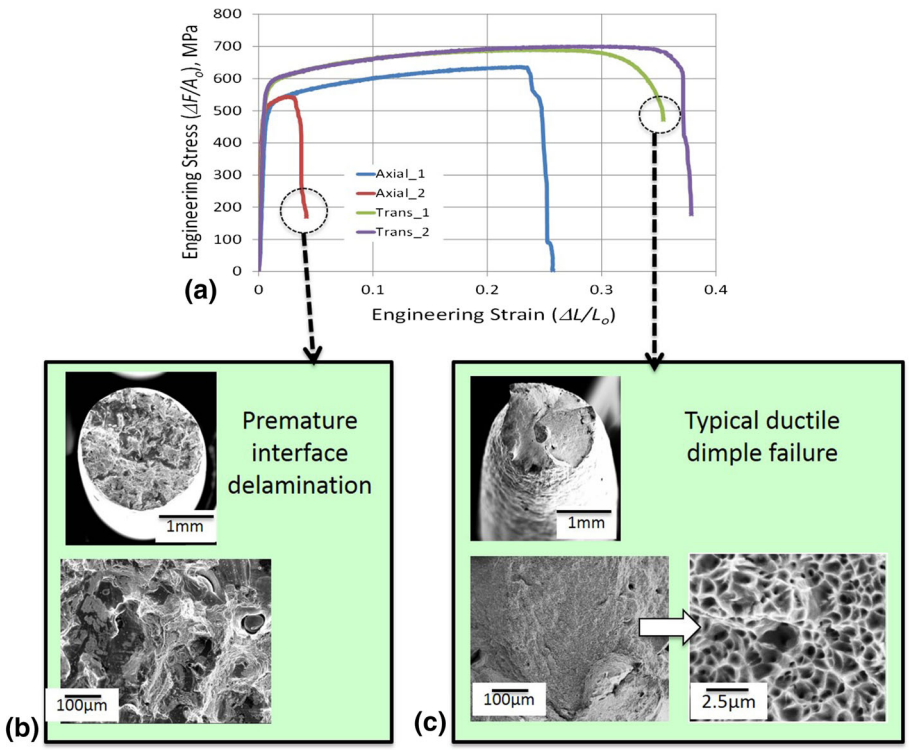

Fig. 30 Correlation between failure mode and tensile property. (a) Stress-strain curve; (b-c) fracture mode for the specimen Axial 2 and Transverse 1, respectively

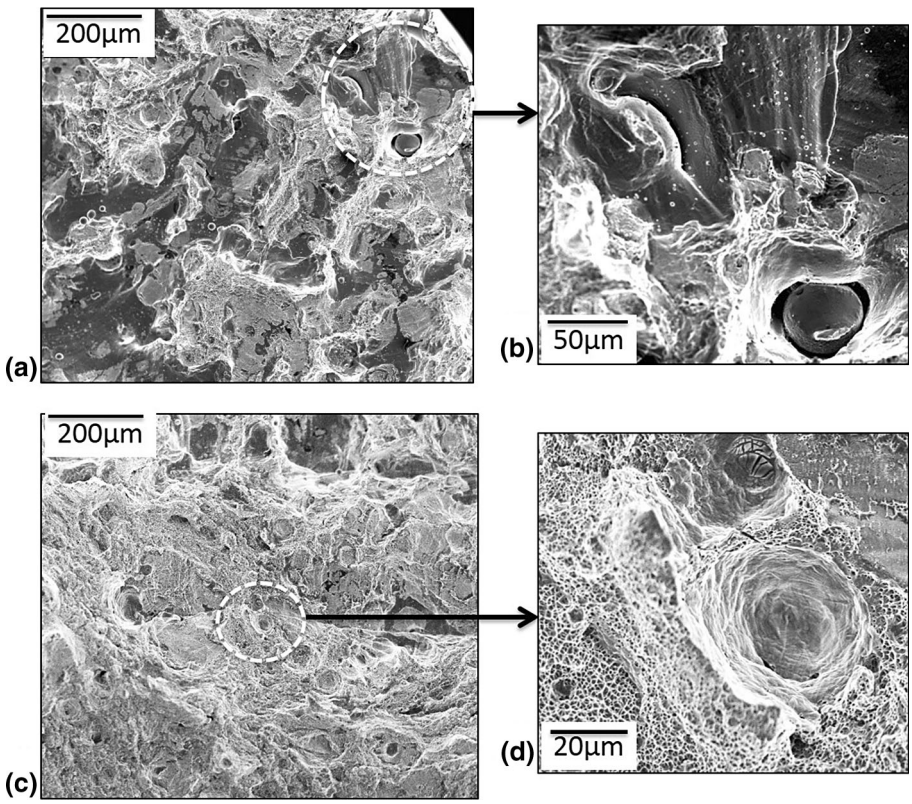

Fig. 31 SEM/SEI micrographs show the tensile failure mode. (a-b) Specimen Axial 1 with increasing magnification; (c-d) Specimen Transverse 1 with increasing magnification

delamination. Some of the coarse ductile dimples were torn around the large interpass inclusions (Fig. 31-lower left). On the other hand, for the Axial #2 specimen with <<10%, strain failed primary by interpass delamination (Fig. 31-upper). It should also be noted that Axial #2 specimen had a high concentration of lack-of-fusion defects at the failed

interpass boundaries, which contributed to its failure as seen in the cross section and fractography of the specimen seen in Fig. 18 and 25, respectively.

Conclusions

The physical metallurgy, microstructure, structural integrity, and therefore ductility of the 3-D LENS prototypes are extremely sensitive to local heat transport and distribution, dictated by the processing parameters and conditions. With properly selected and controlled deposition conditions, the 3-D LENS process is capable of producing a fully dense prototype with high strength and adequate ductility. Inadequate 3-D LENS processing conditions could lead to surface fusion of flying feedstock powder particles during the deposition of each layer. This feedstock powder deposition not only impacts the surface topography, but also causes the material to be vulnerable to gross defect formation at interpass boundaries, which therefore compromises the strength and ductility of the material. To achieve the assurance of the material property and manufacturing consistency, a rigorous study on 3-D LENS process control and optimization, and process simulation and validation must be an integral part of the science and technology maturation effort.

Acknowledgments The authors would like to acknowledge the programmatic support of Paul Spence and Mike Hardwick. Sandia National Laboratories is a multi-program laboratory managed and operated by Sandia Corporation, a wholly owned subsidiary of Lockheed Martin Corporation, for the U.S. Department of Energy's National Nuclear Security Administration under contract DE-AC04-94AL85000.

References

1. ASTM F2792-12a, ASTM, 2012
2. B. Zheng, Y. Xiong, J. Nguyen, J.E. Smugeresky, Y. Zhou, E.J. Lavernia, and J.M. Schoenung, Powder Additive Processing with Laser Engineered Net Shaping (LENS), *Powder Metallurgy Research Trends*, L.J. Smit and J.H. Van Dijk, Ed., Nova Science Publishers, New York, 2009, p 125-190
3. D.D. Gu, W. Meiners, K. Wissenbach, and R. Poprawe, Laser additive manufacturing of metallic compeonts: materials, processes and mechanisms, *Int. Mater. Rev.*, 2012, **57**, p 133-164
4. J.J. Beaman, C. Atwood, T.L. Bergman, D. Bourell, S. Hollister, and D. Rosen, *WTEC Panel Report on Additive/Substractive Manufacturing Research in Europe*, World Technology Evaluation Center, Inc., Baltimore, MD, 2004, p 1-137
5. S.D. Washko and G. Aggen, *ASM Handbook*, Almere, ASM International, 1990, p 841-907
6. M.C. Flemings, *Solidification Processing*, McGraw-Hill, New York, 1974
7. J.F. Lancaster, *Metallurgy of Welding*, Elsevier, Amsterdam, 1999
8. J.A. Brooks and A.W. Thompson, SAND90-8620, (1990).
9. J.A. Brooks and K.W. Mahin, Solidification and Structure of Welds, *Welding: Theory and Practice*, D.L. Olson, R.D. Dixon, and A.L. Liby, Ed., Elsevier, Amsterdam, 1990,
10. J.C. Lippold and D.J. Kotecki, *Welding Metallurgy and Weldability of Stainless Steels*, Wiley, Hoboken, NJ, 2005
11. T.H. Courtney, *Mechanical Behavior of Materials*, 2nd ed., McGraw-Hill, New York, 2000
12. B. Zheng, Y. Zhou, J.E. Smugeresky, J.M. Schoenung, and E.J. Lavernia, Thermal behavior and microstructural evolution during laser deposition with laser-engineered net shaping: Part I. Numerical calculations, *Metall. Mater. Trans. A*, 2008, **39**, p 2228-2236
13. E.W. Reutzel and A.R. Nassar, A survey of sensing and control systems for machine and process monitoring of directed energy, metal-based additive manufacturing, *Rapid. Prototyp. J.*, 2015, **21**, p 159-167
14. W. Hofmeister and M. Griffith, Solidification in direct metal deposition by LENS processing, *JOM*, 2001, **53**, p 30-34
15. B. Zheng, Y. Zhou, J.E. Smugeresky, J.M. Schoenung, and E.J. Lavernia, Thermal behavior and microstructure evolution during laser deposition with laser-engineered net shaping: Part II. Experimental investigation and discussion, *Metall. Mater. Trans. A*, 2008, **39**, p 2237-2245
16. P.J. Maziasz, E.A. Payzant, M.E. Schlienger, and K.M. McHugh, Residual stresses and microstructure of H13 steel formed by combining two different direct fabrication methods, *Scr. Mater.*, 1998, **39**, p 1471-1476
17. M.L. Griffith, M.E. Schlienger, L.D. Harwell, M.S. Oliver, M.D. Baldwin, M.T. Ensz, M. Essien, J. Brooks, C.V. Robino, J.E. Smugeresky, W.H. Hofmeister, M.J. Wert, and D.V. Nelson, *Mater Des*, 1999, **20**, p 107-113